



Does an inter-flaw length control the accuracy of rupture forecasting in geological materials?

Jérémie Vasseur^{a,*}, Fabian B. Wadsworth^a, Michael J. Heap^b, Ian G. Main^c, Yan Lavallée^d, Donald B. Dingwell^a

^a Dept. of Earth and Environmental Sciences, Ludwig Maximilian University, Munich, Germany

^b Institut de Physique de Globe de Strasbourg (UMR 7516 CNRS), Strasbourg, France

^c School of Geosciences, University of Edinburgh, Edinburgh, UK

^d Dept. of Earth, Ocean and Ecological Sciences, University of Liverpool, Liverpool, UK

ARTICLE INFO

Article history:

Received 11 April 2017

Received in revised form 29 June 2017

Accepted 4 July 2017

Available online xxxx

Editor: J. Brodholt

Keywords:

porous materials
inter-pore length
acoustic emission
precursors
rock failure
damage mechanics

ABSTRACT

Multi-scale failure of porous materials is an important phenomenon in nature and in material physics – from controlled laboratory tests to rockbursts, landslides, volcanic eruptions and earthquakes. A key unsolved research question is how to accurately forecast the time of system-sized catastrophic failure, based on observations of precursory events such as acoustic emissions (AE) in laboratory samples, or, on a larger scale, small earthquakes. Until now, the length scale associated with precursory events has not been well quantified, resulting in forecasting tools that are often unreliable. Here we test the hypothesis that the accuracy of the forecast failure time depends on the inter-flaw distance in the starting material. We use new experimental datasets for the deformation of porous materials to infer the critical crack length at failure from a static damage mechanics model. The style of acceleration of AE rate prior to failure, and the accuracy of forecast failure time, both depend on whether the cracks can span the inter-flaw length or not. A smooth inverse power-law acceleration of AE rate to failure, and an accurate forecast, occurs when the cracks are sufficiently long to bridge pore spaces. When this is not the case, the predicted failure time is much less accurate and failure is preceded by an exponential AE rate trend. Finally, we provide a quantitative and pragmatic correction for the systematic error in the forecast failure time, valid for structurally isotropic porous materials, which could be tested against larger-scale natural failure events, with suitable scaling for the relevant inter-flaw distances.

© 2017 Elsevier B.V. All rights reserved.

1. Introduction

All materials contain flaws with a large range of length scales, from kilometre-sized fractures in the crust (Hatton et al., 1994), to meter-sized cavities (Castro et al., 2002) and fractures in rocks and synthetic materials (Allègre et al., 1982), down to micro- and nano-pores and density fluctuations in thin-film glasses (Guyer and Dauskardt, 2004) and crystals. These flawed materials eventually rupture in catastrophic failure events when applied stresses become sufficiently large to produce system-spanning fractures (Sammis and Ashby, 1986). Recent efforts have converged and found that two observations dominate the physics of failure of these systems. First, the flaws in the system concentrate stress relative to the unflawed domains of the material and therefore

the flaw fraction in the material exerts a first-order control on the far-field stress required for macroscopic failure (Kemeny and Cook, 1986; Sammis and Ashby, 1986; Vasseur et al., 2013). Second, the size of flaws and the inter-flaw length determine the extent to which the cracks that emanate from flaws will interfere (Bažant, 2004; Sornette and Andersen, 1998). These two paradigms underpin all elastic models of rupture events in heterogeneous solids and predict that, as the material approaches macroscopic failure, the rate of energy released as acoustic emissions (AEs) by microscopic failure events accelerates (Kilburn, 2012; Lockner et al., 1991; Scholz, 1968; Turcotte and Newman, 2003; Vasseur et al., 2015; Voight, 1989). When first proposed, the finding that these bulk-material accelerations in the rate of energy release or event number approaches a singularity that coincided with the failure time provided a tantalizing possibility that material failure could be forecast accurately using indirect observations such as micro-earthquakes or AEs prior to wholesale rupture

* Corresponding author.

E-mail address: jeremie.vasseur@min.uni-muenchen.de (J. Vasseur).

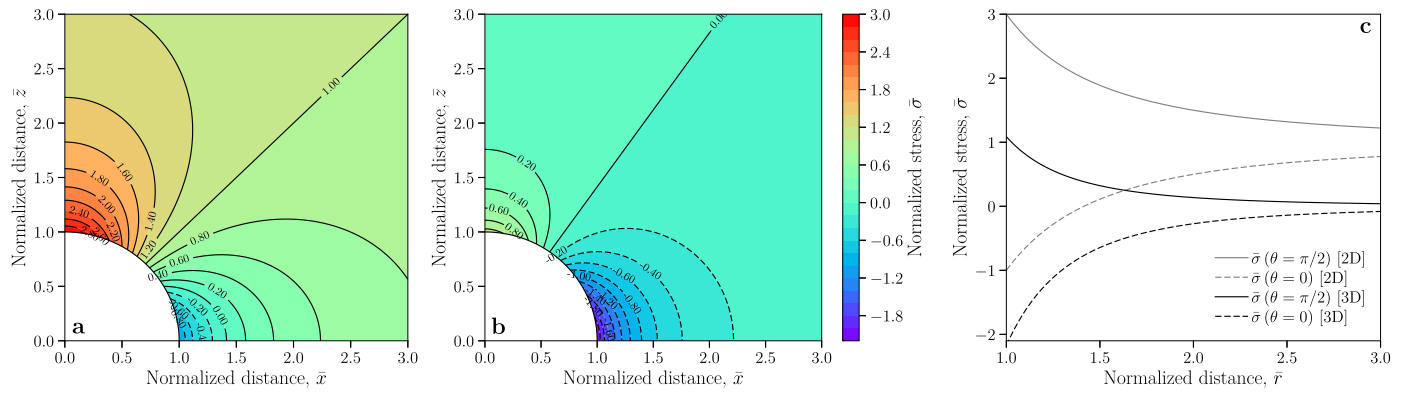


Fig. 1. Stress around pores in 2D and 3D. The distances are normalized by the cavity radius a and the stress by the far-field applied stress σ_1 . (a) The total stress distribution around a circular pore in an infinite plate (2D) mapped out in the positive quadrant of the x - z plane as calculated by combining Eqs. (S1)–(S3). (b) The total stress distribution around a spherical pore in an infinite body (3D) mapped out in the positive quadrant of x - z plane as calculated by combining Eqs. (S4)–(S7). (c) The total stress resolved along the z -axis ($\theta = \pi/2$) and along the x -axis (2D) or the x - y plane (3D) ($\theta = 0$).

(Voight, 1989). Indeed a large effort has been expended in assessing the utility of this tool for forecasting hazardous failure phenomena in nature (Bell et al., 2011; Bell and Kilburn, 2013; Hao et al., 2016; Kilburn et al., 2017; Robertson and Kilburn, 2016; Voight, 1988). However, the still-limited success of these methods (Bell et al., 2013) has highlighted complexities in the approach to failure of heterogeneous materials that must be addressed if forecasting tools are going to be of the widest utility.

2. Micromechanical models for the uniaxial deformation of porous materials

Here we present a linear elastic model to demonstrate quantitatively how stress is distributed around a circular (2D) or spherical (3D) cavity in an infinite solid and exposed to a far-field stress. Then we follow previous work to scale that concept to a porous body with finite dimensions in order to predict the failure stress of a porous material as a function of the porosity ϕ and the pore radius a . We focus on the uniaxial case in which far-field stresses are applied in one direction only, and later we discuss how our findings could be extended to more complex stress configurations in principle. Finally, we explore other characteristic length scales in natural materials that may be more relevant than the pore size; namely, the inter-pore and inter-particle distances.

2.1. The concentration of uniaxial applied stress around circular and spherical pores

First we use a linear elastic model for the stress distribution around a circular (2D) or spherical (3D) cavity. For the 2D case we opt for the solution credited to Kirsch (1898) and to Goodier (1933) for the 3D case, repeated in variable completeness in subsequent work (Jaeger et al., 2009; Soutas-Little, 1999) with which the stress components can be computed for each spatial position around a cavity of radius a . We use the Cartesian coordinate system with the far-field stress applied in the z -direction and the centre of the pore positioned at $(x, y, z) = 0$. A line of length r away from the pore centre in any direction subtends an angle with the z -axis of θ and an angle with the x - or y -axes of ψ . In what follows, we normalize each axis (x, y, z) and the radial direction r by a and the individual stress components τ_{ij} by the far-field applied stress σ_1 , yielding a coordinate system and stress tensor components for which a bar above the parameter denotes its normalized value. We introduce the 2D and 3D stress components in the supplementary file as Eqs. (S1)–(S3) and Eqs. (S4)–(S7).

In Fig. 1, we present the normalized stress as a colour map around a 2D circular cavity (Fig. 1a) and a 3D spherical cavity using $\nu = 0.25$ (Fig. 1b), which is a first-order approximation for crustal rocks (assuming the two Lamé parameters are equal). The lobes of concentrated stress are compressive in the region of the solid surrounding the z -axis and are tensile in the region of the solid about the x -axis (2D) or the x - y plane (3D). It is in these lobes of concentrated stress that fractures would be most likely to initiate. For this reason, in Fig. 1c we additionally show the stress resolved along the z -axis ($\theta = \pi/2$) and along the x -axis (2D) or the x - y plane (3D) ($\theta = 0$).

2.2. Approximate methods for predicting the stress required for rupture

The deformation of elastic porous media results in cracks that propagate from interfaces at which stress is locally concentrated relative to the far-field applied load (Sammis and Ashby, 1986). Sammis and Ashby (1986) present a static so-called *pore-crack* model to compute the degree to which stress is concentrated around cavities (a cavity stress intensity factor K_{ji}) and the degree to which cracks that grow from those cavities interact (a crack interaction stress intensity factor K_{jii}). Their solutions are cast as simple functions of the sample porosity ϕ , rendering them easy to use and to compare with measured data (Zhu et al., 2011). Where the *pore-crack* model is used, only the solution for 2D is usually compared with experimental data (Baud et al., 2014; Zhu et al., 2011). Here we apply the *pore-crack* model (Sammis and Ashby, 1986) in uniaxial conditions where the sum of K_{ji} and K_{jii} is the total stress intensity K_I .

When a far-field stress σ_1 is applied ($\sigma_2 = \sigma_3 = 0$) onto a material rupture begins only when the local stress σ exceeds σ_c . At this point a fracture can initiate to a distance c away from the pore or cavity at which distance $\sigma = \sigma_c$, and beyond which $\sigma < \sigma_c$. This distance c is the equilibrium crack length for the stress state at a given time and, defined in non-dimensional form as $\bar{c} = c/a$. Then \bar{c} as a function of a normalized stress $\bar{\sigma} = \sigma\sqrt{\pi a}/K_{Ic}$ (where K_{Ic} is the fracture toughness or critical stress intensity required for crack propagation in the solid) for the 3D and uniaxial case, is as follows (Sammis and Ashby, 1986)

$$\bar{\sigma} = \left(\frac{0.62\sqrt{\bar{c}}}{(1+\bar{c})^{4.1}} + \frac{\sqrt{2\phi(1+\bar{c})}}{\pi} \right)^{-1} \quad (1)$$

where the first term on the right-hand side of Eq. (1) describes the growth of a crack from a single pore, while the second term is a crack-interaction term related to the porosity ϕ (see Sammis and Ashby, 1986 for full description). This model neglects time-dependency and therefore it is implicitly assumed that the cracks

grow more quickly than the far-field stress changes. This is similar to saying that the strain rate is sufficiently low that the damage is in equilibrium with the stress at all times.

Eq. (1) provides us with a tool to assess when linear elastic mechanics predicts failure for a porous material loaded uniaxially by assessing Eq. (1) when $d\bar{\sigma}/d\bar{c} = 0$. This condition clearly demarks the onset point beyond which increased crack growth will manifest as a stress drop. In practice, the sample can remain coherent for a relatively small region of crack lengths above this point, but, following Zhu et al. (2011), we approximate the failure point as described. At this point, we can define the equilibrium normalized crack length that is failure in this model as $\bar{c}_c = c_c/a$ where \bar{c}_c is a function of ϕ only. Differentiating Eq. (1) with respect to \bar{c} and setting $d\bar{\sigma}/d\bar{c} = 0$ then yields an expression for the porosity

$$\phi = 2\pi^2(1 + \bar{c}_c) \left(\frac{2.542\sqrt{\bar{c}_c}}{(1 + \bar{c}_c)^{5.1}} - \frac{0.31}{(1 + \bar{c}_c)^{4.1}\sqrt{\bar{c}_c}} \right)^2 \quad (2)$$

so that the equilibrium crack length at failure \bar{c}_c can be found numerically for a given ϕ .

2.3. The inter-flaw length and pore sizes in porous materials

In natural rocks as well as synthetic porous materials, the pore space is rarely an array of spherical cavities (e.g. Vasseur et al., 2013). Indeed, for sandstone, limestone, welded volcanic materials including ignimbrites, among many other lithologies, it is more relevant to think of the solid matrix as an array of near-spherical objects (grains) and the pore space as the convolute inter-sphere void (Vasseur et al., 2016). In this scenario, we can apply metrics for the characteristic length scales of the system based on theoretical models for the description of microstructure in random heterogeneous materials (Torquato, 2013). This is an advance on using simple concepts of “pore sizes”, which are typically scaled to bulk porosity simply by assuming regular simple arrays of monodisperse pores in a unit volume (Zhu et al., 2011).

If we think of our model geological material as a packing of spherical grains with radius R and that these grains are able to freely overlap or inter-penetrate, then we can account for porosities lower than the maximum packing porosity of grains. In this case, we use a nearest-neighbour function to find the average inter-pore lengths in a heterogeneous grain pack. The nearest-neighbour function in a random system of interacting spheres can be evaluated from the probability $F(r)dr$ that an arbitrary sphere centre in the system lies at a distance between r and $r + dr$ from another sphere centre. The n th moment of $F(r)$ is given by (Torquato et al., 1990)

$$\langle \bar{r}^n \rangle = \int_0^\infty \bar{r}^n \bar{F}(\bar{r}) d\bar{r} \quad (3)$$

where a bar above a symbol denotes a parameter normalized by the sphere radius \mathcal{R} (i.e. $\bar{r} = r/\mathcal{R}$ and $\bar{F}(\bar{r}) = F(r)\mathcal{R}$). The first moment (i.e. $n = 1$) gives the mean nearest-neighbour distance between spheres $\bar{l} \equiv \langle \bar{r} \rangle$. In our case the spheres can either represent the pores (i.e. $\mathcal{R} = a$), yielding inter-pore distances termed l_1 , or the particles (i.e. $\mathcal{R} = R$), yielding inter-particle distances termed l_2 . In the case where the spheres are monodisperse and fully penetrable, the nearest-neighbour function for finding l_1 or l_2 is (Torquato et al., 1990)

$$\bar{F}(\bar{r}) = 3\eta\bar{r}^2 \exp(-\eta\bar{r}^3) \quad (4)$$

where η represents the sphere reduced density (i.e. the product of sphere number density and sphere volume). Combining Eq. (4) with Eq. (3) and taking $n = 1$, results in an analytical expression

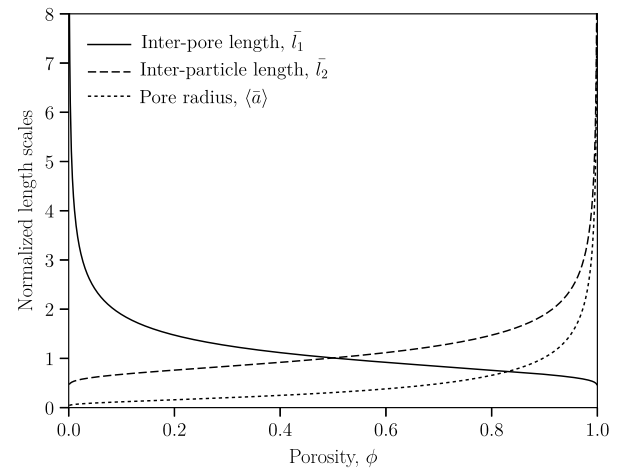


Fig. 2. The calculated mean nearest-neighbour distance between overlapping spheres in a statistically random heterogeneous medium as a function of porosity using Eqs. (5) and (7). l_1 corresponds to the case where the spheres are the pores (porosity is thus the sphere volume fraction) and is then an inter-pore distance. l_2 corresponds to the inverse case where the spheres are the particles (porosity is thus the volume fraction exterior to the spheres) and is then an inter-particle length. (a) corresponds to the mean pore radius between solid spheres.

$$\bar{l}_i = \frac{\Gamma(4/3)}{\eta^{1/3}} \quad (5)$$

where Γ is the gamma function, and $\eta = -\ln(1 - \phi)$ when $i = 1$ (the case when $\bar{l}_1 = l_1/a$) and $\eta = -\ln\phi$ when $i = 2$ (the case when $\bar{l}_2 = l_2/R$). We can think of l_1 as a characteristic inter-pore distance which we will use to estimate the average distance a crack must bridge to connect two pores, and l_2 as a characteristic inter-particle distance which we can think of as a more rigorous proxy for pore size in heterogeneous random media. In Fig. 2 we show how both \bar{l}_1 and \bar{l}_2 vary with ϕ for overlapping monodisperse spheres (spherical pores in the case of \bar{l}_1 and spherical particles in the case of \bar{l}_2).

For comparison, we can also use the model of Lu and Torquato (1992) to predict the characteristic pore radius between random heterogeneous overlapping particles. To do this, we use Eq. (4) to get a pore-size density function $P(a)$ (here $\eta = -\ln\phi$)

$$\bar{P}(\bar{a}) = \frac{\bar{F}(1 + \bar{a})}{\phi} = \frac{3\eta(1 + \bar{a})^2}{\phi} \exp(-\eta(1 + \bar{a})^3) \quad (6)$$

where $\bar{a} = a/R$ and $\bar{P}(\bar{a}) = P(a)R$. The n th moment of $P(a)$ is given by

$$\langle \bar{a}^n \rangle = \int_0^\infty \bar{a}^n \bar{P}(\bar{a}) d\bar{a} \quad (7)$$

and the first moment (i.e. $n = 1$) gives the mean pore radius $\langle \bar{a} \rangle$.

3. Experimental materials and methods

3.1. Materials, experimental deformation and data acquisition

We use experimental data from samples of a range of different porous geological media including sandstone, limestone, volcanic welded debris, and synthetic analogues for quartz-rich sandstone of sintered glass beads (cf. Blair et al., 1993). While these data are associated with experiments from published studies (Heap et al., 2013, 2015; Wadsworth et al., 2016), the acoustic data are analysed here for the first time in terms of the critical crack length inferred from a micromechanical model. Fig. 3 shows photomicrographs of characteristic sample microstructure collected either

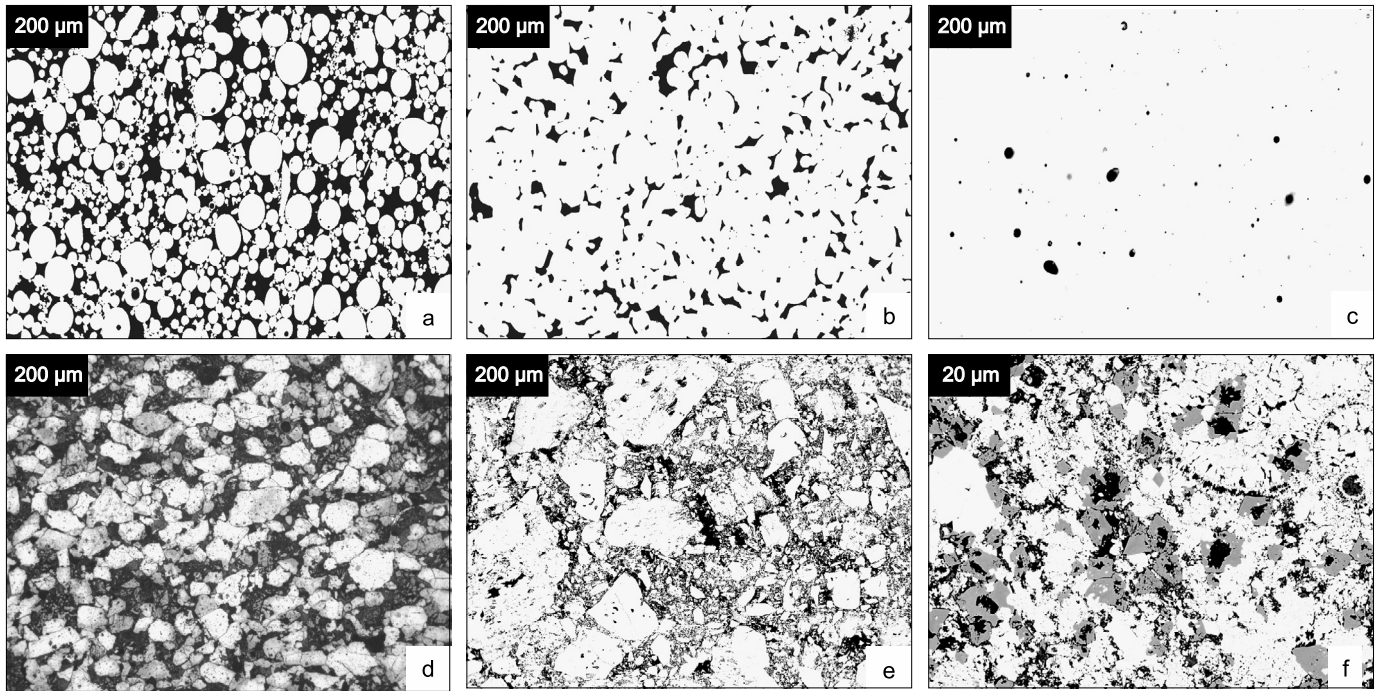


Fig. 3. Characteristic photomicrographs of the samples used in this study: a suite of (a)–(c) synthetic porous glasses and (d)–(f) natural samples. Black represents the gas phase, white and shades of grey the solid phase. (a)–(c). Sintered glass beads from Vasseur et al. (2015) with varying porosity. (d) Darley Dale (UK) sandstone from Wadsworth et al. (2016). (e) Mt Meager (Canada) welded volcanic debris from Heap et al. (2015). (f) Mt Climiti (Italy) carbonate from Heap et al. (2013). Note that all materials are porous, variably densified, initially granular materials with simple microstructures (a)–(c) or increasingly complex microstructures (d)–(f). In particular, the limestone (f) is multiphase and finer grained than the other samples (a)–(e).

using scanning electron microscopy or optical microscopy. We selected this range of samples to encompass the simplest case of a two-phase system of solid and pores (synthetic analogues for quartz-rich sandstones; Fig. 3a–c), and the more complex cases of multiphase natural materials relevant to crustal rocks (quartz-rich sandstones, volcanic clastic rocks, and clastic limestones; Fig. 3d–f).

The porosity of all materials was determined using helium pycnometry and the mean particle sizes ($\langle R \rangle$) were estimated using optical microscopy. For the sandstone samples $\langle R \rangle \approx 2.5 \times 10^{-4}$ m (Wadsworth et al., 2016), for the limestone samples $\langle R \rangle \approx 2.5 \times 10^{-4}$ m (Heap et al., 2013), for the welded volcanic debris $\langle R \rangle \approx 2 \times 10^{-4}$ m (Heap et al., 2015), and for the synthetic sintered glass beads, $\langle R \rangle \approx 7.6 \times 10^{-5}$ m (Vasseur et al., 2016, 2015). All samples were dried and deformed under uniaxial loading at a constant strain rate of 10^{-5} s $^{-1}$. Acoustic emission data was collected continuously during deformation at acquisition rates of 20 MHz, synchronized with the mechanical data acquisition.

In uniaxial tests, the time at which the samples rupture completely, t_c , is simply the point at which the measured stress drops significantly and is therefore trivial to pick. At a strain rate of 10^{-5} s $^{-1}$ the peak stress σ_c typically occurs at $t = t_c$ or just prior to t_c , consistent with the failure criterion $d\bar{\sigma}/d\bar{c} = 0$ assumed above in deriving Eq. (2).

3.2. Retrospective ‘forecasting’ of the failure time

Retrospective forecasting, or ‘hindcasting’ is a necessary though not sufficient step in assessing the predictability of non-linear complex systems. It can provide a ‘best-case scenario’ for forecasting in prospect near the failure time, but can also provide insight into phenomena not yet included in current models. Here we test a commonly-applied model for failure forecasting using precursory changes in the rate of acoustic emissions – high-frequency elastic wave packets generated by the rapid release of strain energy during local micro-crack rupture – during deformation. Specifically, we monitor the number of events per unit time $\dot{\Omega}$, the parameter

most commonly used to forecast failure of a system due to its sensitivity to deformation (Lavallée et al., 2013, 2008; Vasseur et al., 2015; Voight, 1988). The variety of lithologies tested allows us to study failure forecasting in a controlled manner, and to isolate the fundamental controls on the evolution of $\dot{\Omega}$ and the accuracy of the forecast failure time.

One of the most common ways to relate the rate of an observable signal $\dot{\Omega}$ that is precursory to the forecast failure time t_p is the Time-Reversed Omori Law (TROL; Vasseur et al., 2015)

$$\dot{\Omega}(t) = k(t_p - t)^{-p} \quad (8)$$

where k is a scaling factor and p parameterizes the rate of acceleration of $\dot{\Omega}$. Here the approach of $\dot{\Omega}$ to failure is an inverse power-law, with a well-defined singularity at t_p , as expected for a system approaching a critical point defined by a system-sized event. Note that in the following we refer to t_c as the observed failure time. Following the procedure described in detail in Bell et al. (2013) we applied the TROL to catalogues of AE events in order to retrospectively forecast failure. This law has three free parameters (k , p and t_p) to adjust, which are not known *a priori*. The Maximum Likelihood (ML) method is applied to the TROL and has been shown to provide statistically stable and repeatable estimates of its parameters (Bell et al., 2013). Additionally, this method uses the timing of individual AE events rather than event rates determined in equally spaced bins (as is commonly the case when applying standard failure forecast methods). The ML solution is found by minimizing the negative log-likelihood function using a downhill simplex algorithm. In an interval (t_0, t_1) and for n number of observations, the log-likelihood function for the TROL is given by

$$\ln(L) = \sum_{i=1}^n \ln(k(t_p - t_i)^{-p}) + \frac{k}{1-p} ((t_p - t_1)^{1-p} - (t_p - t_0)^{1-p}) \quad (9)$$

for $p \neq 1$ and

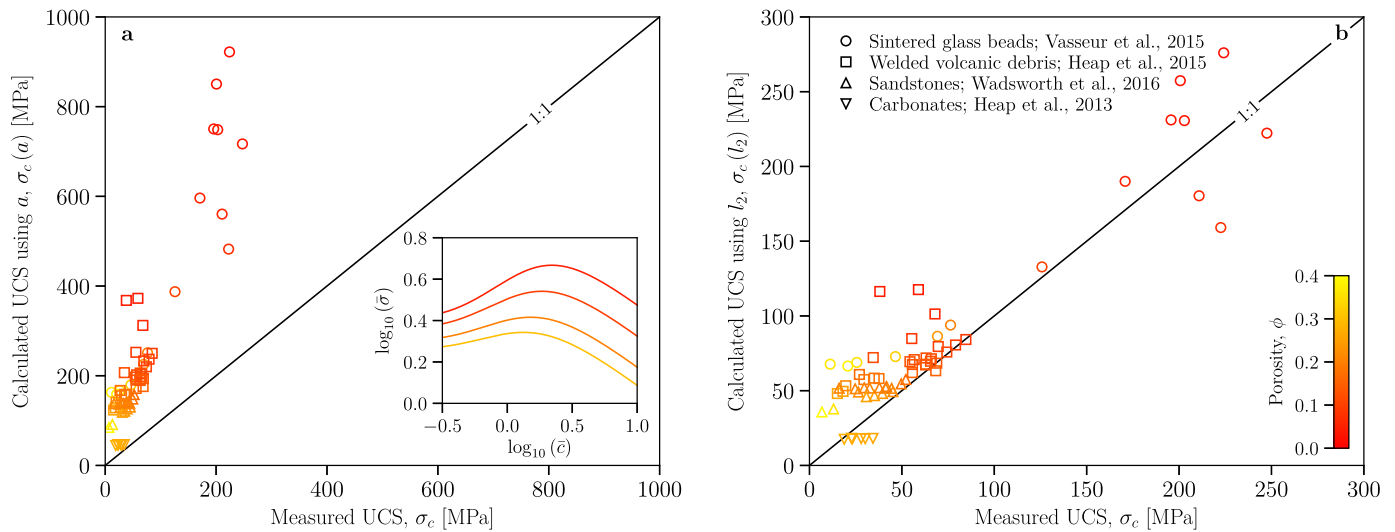


Fig. 4. Calculated versus measured uniaxial compressive strength (UCS) using (a) the inferred mean pore radius (a) from Eq. (7) and (b) the inferred inter-particle distance l_2 from Eq. (5) for all the samples studied here and colour-coded for porosity. *Inset* – the evolution of stress σ with crack length c for 4 different porosity values as calculated from Eq. (1) for a sample subjected to uniaxial loading.

$$\ln(L) = \sum_{i=1}^n \ln(k(t_p - t_i)^{-1}) + k(\ln(t_p - t_1) - \ln(t_p - t_0)) \quad (10)$$

for $p = 1$. This yields a retrospective forecasted failure time t_p based on precursory signals only.

Alternatively, the approach of $\dot{\Omega}$ to failure may be exponential: $\dot{\Omega}(t) = h \exp(qt)$, where h is another scaling parameter and q controls the evolution of $\dot{\Omega}$. The exponential model can be fit in the same way using another form of the ML method but does not have the same degree of forecast power as there is no unambiguous singularity in $\dot{\Omega}$ at any time. The ML solution for the exponential law is

$$\ln(L) = q \sum_{i=1}^n t_i + n \ln(h) - \frac{h}{q} (\exp(qt_1) - \exp(qt_0)) \quad (11)$$

The forecasting window was restricted to 90% of the known failure time t_c . In cases where the TROL is an appropriate model for the underlying process, the analysis by Bell et al. (2011) indicates a typical random error (precision) of $\pm 6\%$ at 95% confidence or so when the forecast was made at 90% of t_c . Hence any difference between forecast and observed t_c above $\pm 6\%$ or so is diagnostic of a systematic error or bias (loss of accuracy) at this level of confidence, requiring a correction to the TROL.

The Bayesian Information Criterion (BIC) is a statistical tool to quantify the relative performance of different models in describing a dataset (i.e. when making an inference, the preferred model is more likely to have the lower BIC value). It is based on the likelihood L of the observation given the model, with a weighting favouring the model with fewer parameters, and is given by $BIC = -2 \ln(L) + N \ln(n)$ for which N is the number of free parameters. Therefore, calculating the positive difference ΔBIC between the BIC value of the TROL and the exponential law respectively helps discriminate which is the preferred model. As such, when the ΔBIC becomes negative it indicates a strong statistical preference for the TROL over the exponential law.

4. Results and analysis

4.1. Comparing results with the mechanical model

Using the peak stress σ_c observed in the uniaxial compression experiments, we can test the micromechanical model presented.

Applying Eq. (1) allows us to compute the normalized uniaxial stresses for every normalized crack length value for a given porosity (see Fig. 4a inset for this result for four porosities). We can compute the normalized critical crack length \bar{c}_c for a failure to occur in a sample of given porosity using Eq. (2), and then convert that to a critical peak stress required for failure $\bar{\sigma}_c$ using Eq. (1). The model and observed peak stresses can then be compared directly as a hypothesis test. As we know the mean particle radius for all of our experimental samples, we can compute a characteristic pore radius using either Eq. (5) to find l_2 or Eq. (7) to find a . We can use this to find the stress required for failure, termed the uniaxial compressive strength (UCS). In Fig. 4 we show that when we perform this analysis using a in the dimensional result for c_c and σ_c , the model performs poorly (Fig. 4a). Whereas when we use δl_2 (with a calibrated $\delta = 3/2$) in the result, we find that the predicted peak stress is in good agreement with the observed peak stress (Fig. 4b). This validates the micromechanical model used here (Sammis and Ashby, 1986), and confirms l_2 as the best metric for the characteristic pore dimension. This is in contrast with previous work in which investigators use a characteristic pore radius a in Eq. (2) (Zhu et al., 2011). The success of using l_2 (Fig. 4b), demonstrates that the challenges associated with defining and measuring l_2 in rocks can be circumvented and represents an advance on previous approaches.

4.2. Predicting the rupture time

We show in Fig. 5 that all samples exhibit apparent acceleration of $\dot{\Omega}$ toward the observed failure time t_c . Here we normalize the time data so that deformation begins at -1 , and t_c occurs at 0 (Fig. 5). Across the full range of porosities tested, these accelerations are well-fit by a power-law TROL (see Eq. (8)). While we plot the cumulative number of events for the model and observed data in Fig. 5, the model was fitted on the rate data, so that the data points remain independent. Here we do not show explicitly the best-fit p , which lie below 1 and compare favourably with previously published values for synthetic tests (Bell et al., 2013) and deformation experiments (Cornelius and Scott, 1993; Voight, 1989). The best-fit t_p diverges from t_c as $\phi \rightarrow 0$, indicating that the power-law extends systematically beyond t_c toward its singularity at $t_p > t_c$. The time deficit between the forecast and observed failure time exceeds the estimated precision of $\pm 6\%$ or so described above, and increases systematically as porosity de-

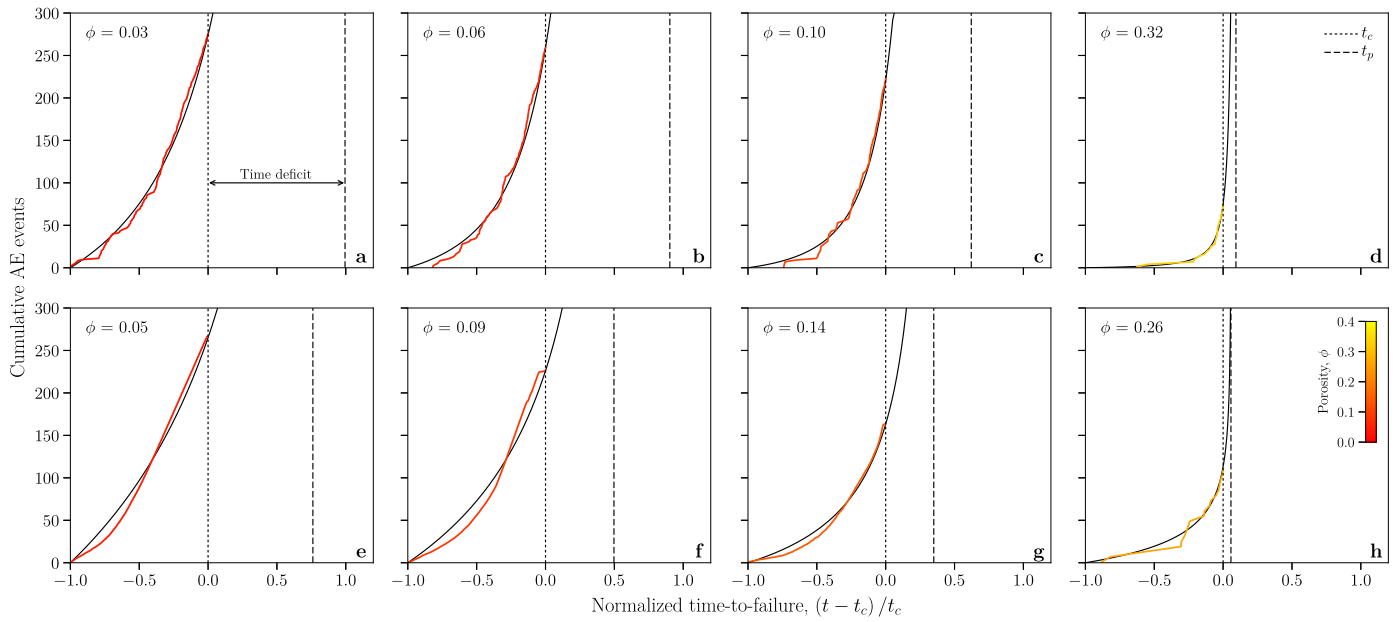


Fig. 5. Examples of failure forecasting for two sample types studied herein (a)–(d) sintered glass beads; Vasseur et al., 2015 and (e)–(h) welded volcanic debris; Heap et al., 2015) with varying porosity. The colourful thick solid lines represent the raw data, while the black thin solid lines represent the model output. The predicted (from the model) t_p and the actual failure times t_c are marked by vertical dashed and dotted lines, respectively. One can notice how the time deficit between t_p and t_c reduces as porosity increases and how this corresponds well with a decrease in distance deficit as shown in Fig. 7.

creases: the systematic error is as high as 100% at a porosity of 3% (Fig. 5).

The observation in Fig. 5 is consistent with those of Vasseur et al. (2015; data from this study is repeated here for context and comparison) and Jiang et al. (2016), whereby system-sized failure can only forecast failure accurately (i.e. within the calculated precision of the ML method) in highly heterogeneous, porous samples. Conversely it does not provide accurate forecasts of failure in relatively homogeneous, low-porosity materials. Vasseur et al. (2015) also showed that failure of porous materials is best described by an inverse power-law acceleration at high porosity, and by the exponential acceleration at low porosity ($\phi < 0.3$; Fig. 6 inset). However, the low-porosity trends are not necessarily exponential in nature and this is an effect of the non-existence of a power-law singularity in these data. Additionally the failure time is not defined by the dynamics underlying the exponential model and failure forecasts using this model must be based on other metrics. These observations highlight a current shortcoming in our ability to forecast system-sized material failure in natural and synthetic porous media, which we now address.

The first clue to accounting for the systematic bias in the failure time is illustrated in Fig. 7a. Here we see a strong positive correlation between the bias, expressed as the ratio of the predicted to the observed failure time, and the inter-pore distance $\bar{l}_1(\phi)$. This implies that failure is poorly resolved when the distance between two pores is large and thus that the crack-length required to connect two pores should also be large. If we apply the micromechanical model used to accurately predict the failure stress, we would expect that $2c_c$ is the crack length required to connect two pores (given that a crack grows from each pore at the same time; dashed line in Fig. 7b). But as porosity decreases, there is a systematic deviation from the micromechanical model result for $\bar{c}_c(\phi)$ from $\bar{l}_1(\phi)$, calculated using Eqs. (2) and (5) respectively. We find a correlative relation between the normalized failure forecast and the normalized critical crack length, such that $t_p/t_c \approx 2\bar{c}_c/\delta$ (with $\bar{c}_c = c_c/l_2$) and hence t_p/t_c as a function of \bar{l}_1 (solid line in Fig. 7b). We infer that this represents a distance deficit between the crack length and the length required to connect two pores, which is larger for low porosity samples than for

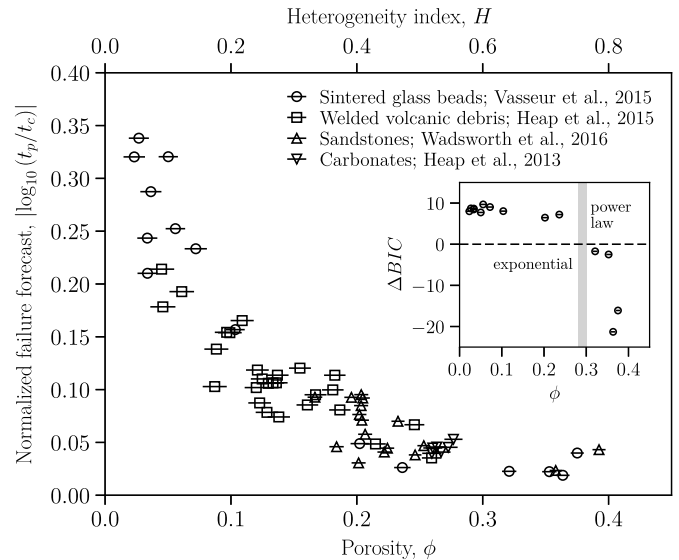


Fig. 6. The dependence of the forecast error (cast as the ratio between the predicted failure time t_p from the TROL and the observed failure time t_c) on the sample porosity ϕ (or heterogeneity index H defined in Vasseur et al., 2015) for a range of rock types and material analogues (Heap et al., 2013, 2015; Vasseur et al., 2015; Wadsworth et al., 2016). Inset – the transition from an exponential to a power law approach of the acoustic emission rate to failure on a statistical basis (see text for definition of the statistical ΔBIC criterion). The vertical grey bar marks the approximate transition between a power-law and an exponential approach to failure and is the same as in Fig. 7.

high porosity samples. We note a strong correlation between this increasing distance deficit (between the dashed and solid lines in Fig. 7b) and the increasing forecast bias with respect to decreasing porosity previously illustrated in Fig. 5. The implication is that low porosity materials have relatively large distances that must be spanned by cracks in order to fail, and that this leads to late time, rapid time-dependent crack growth rather than equilibrium crack growth predicted by the static model here presented. This also seems to correlate with the shift from AE accelerations that

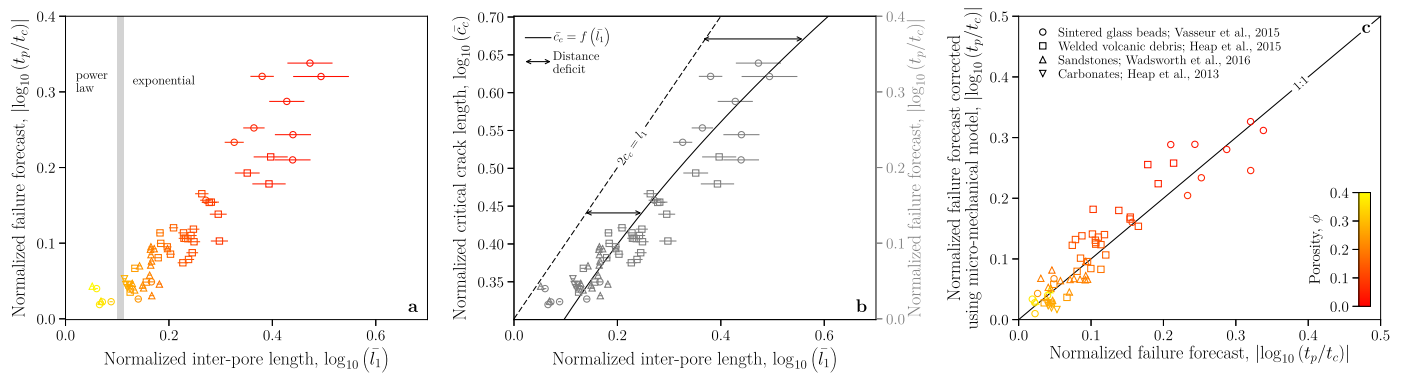


Fig. 7. Testing the micromechanical origin of errors in failure prediction. (a) The ratio between the predicted failure time t_p from the TROL and the observed failure time t_c as a function of the normalized mean nearest-neighbour length \bar{l}_1 . The vertical grey line represents the transition between low \bar{l}_1 where the acoustic emission output as failure is approached is a power-law and high \bar{l}_1 where this approach to failure is an exponential function (see Fig. 6 inset). (b) The equilibrium crack lengths at failure from a micromechanical model for deformation of porous solids compared with the mean nearest-neighbour length (solid line calibrated in Fig. 2; Sammis and Ashby, 1986). Shown for comparison are the data from panel (a) (grey data) showing that the failure forecast discrepancy grows as the critical crack length at failure becomes less than the half-distance between pores. (c) The empirical correction proposed herein provides well-resolved failure forecasts.

are well-predicted by power laws (and accurately forecast failure) to those that are better predicted by exponential accelerations and which cannot accurately forecast failure.

Finally, we use the distance deficit of Fig. 7b to correct for the bias in the forecast failure time, as illustrated in Fig. 7c. The agreement is very good within the remaining (random) scatter in the data about the optimal line. This figure validates the modification to the TROL we have made using the microstructural and micromechanical models presented, and the empirical results of Figs. 7a and 7b.

5. Discussion and conclusions

Our work shows that as the nearest-neighbour distance approaches the pore size, i.e. $\bar{l}_1 \rightarrow 1$, the forecast failure time becomes more accurate, and that this transition can be associated with the case where $2\bar{c}_c = \bar{l}_1$. More specifically, if the equilibrium crack length at failure approaches half the total distance between pores which must be bridged to achieve failure, then the precursory AE rate indeed exhibits an inverse power law approach to a critical singularity that coincides with the observation of catastrophic failure. However, when the nearest-neighbour distance is much greater than the pore size $\bar{l}_1 \gg 1$, then the forecast is not successful and there is a length-deficit between the equilibrium crack length \bar{c} and the distance that must be bridged \bar{l}_1 . This implies that there is not a simple approach to a critical failure point for systems in which there is a length-deficit: instead failure occurs suddenly and early. This is consistent with the observation that the approach to failure is better described by an exponential than a power-law evolution in the AE rate on a statistical basis for these samples (Fig. 6 inset). Finally, this finding suggests that it is the inter-pore length (the nearest-neighbour distance) that is more important than the porosity of a medium in determining whether a crack can propagate the required half-distance between two neighbouring pores to precipitate failure.

Although we focus on the uniaxial loading case for experimental convenience, the full triaxial micromechanical model provided by Sammis and Ashby (1986) could be used to extend the results to the compressional stress field relevant to the Earth's crust. There is no reason to anticipate a distance deficit term would not act as a control on the early failure time in this case, though this may take a different functional form to the results presented here, which itself may be dependent on confining pressure. This remains to be tested in future work. We also note the materials here tested are structurally isotropic, so there is no directional dependence of the inter-pore length scaling. This is not necessarily true at all scales in

natural and synthetic systems, so the effect of anisotropy remains to be examined.

There is large variability in the accuracy and reliability of forecast attempts using the classic failure forecast method (De la Cruz-Reyna and Reyes-Dávila, 2001; Kilburn, 2003; Kilburn and Voight, 1998; Ortiz et al., 2003; Smith et al., 2007; Smith and Kilburn, 2010; Voight and Cornelius, 1991) or the TROL (Bell et al., 2013) or variations thereof (Boué et al., 2015; Salvage and Neuberg, 2016). This applies even for fully retrospective forecasting of volcanic eruption time, based on precursory earthquakes at different volcanoes worldwide. This demonstrates that there is a wide range of error in applying this method to natural data, and that these tools are not always of the widest utility for real time monitoring. While we have proposed a correction that works well in a controlled laboratory setting, it is unlikely that pore-scale heterogeneity controls volcano- or fault-scale rupture. However, it is likely that there are larger length scale domains of heterogeneity in those crustal systems, which control the flaw-to-flaw fracture propagation events precursory to system-sized rupture. Our model therefore suggests that if these larger scale flaws can be identified, then it is their inter-flaw distances that would most likely scale the error in forecasts. Nevertheless, in qualitative terms, our model suggests that it is the most apparently heterogeneous systems, with the lowest inter-flaw distances, that might be expected to be well forecast using the variants of the failure forecasting method outlined above. One example could be the Mt St Helens volcano (USA) in 1985–1986, which had a systematic error in the forecast failure time of <0.1 expressed as a time since the start of the acceleration (Voight and Cornelius, 1991).

In the volcanic case, there is a crucial distinction to be drawn between events that can be interpreted to be the result of magma fracturing during ascent (Kendrick et al., 2014; Neuberg et al., 2006) in an established conduit and those that are likely related to the fracturing of crustal rocks during the initiation of eruption and magma propagation to the surface (Kilburn et al., 2017; Lamb et al., 2017). An example of the latter interpretation was made on the basis of the patterns of evolution of low-frequency events preceding individual eruption episodes at Soufriere Hills volcano (Montserrat) (Neuberg et al., 2006), and an example of the latter is the signal evolution without eruption at Campi Flegrei (Italy) (Kilburn et al., 2017). Our experiments are explicitly suited to explain the brittle mechanics involved in the latter process of crustal fracturing ahead of a vanguard magma batch on its way to the surface. But additionally, our results are applicable to the highest viscosity systems in the former case of fracturing of magma itself (Lavallée et al., 2008).

In summary this study provides a simple explanation for the substantial variability in the success of forecast attempts for system-sized catastrophic failure in natural and artificial systems (Bell and Kilburn, 2013, 2012) and the quantitative correction we provide offers the opportunity to scale lab-forecasts to natural systems, if a convincing scaling for lengths between large scale flaws can be identified.

Acknowledgements

Funding was provided by a European Research Council (ERC) Advanced Grant on Explosive Volcanism in the Earth System: Experimental Insights (EVOKES, No. 247076), a ERC Starting Grant on Strain Localisation in Magma (SLiM, No. 306488), a German Research Foundation (DFG) Grant (No. LA-2651/1-1), and a Franco-German Partenariat Hubert Curien (PHC) Procope Grant (No. 332065SG). We thank two anonymous reviewers for their thoughtful and constructive feedback on an earlier version of the manuscript.

Appendix A. Supplementary material

Supplementary material related to this article can be found online at <http://dx.doi.org/10.1016/j.epsl.2017.07.011>.

References

- Allègre, C.J., Le Mouél, J.L., Provost, A., 1982. Scaling rules in rock fracture and possible implications for earthquake prediction. *Nature* 297, 47–49. <http://dx.doi.org/10.1038/297047a0>.
- Baud, P., Wong, T., Zhu, W., 2014. Effects of porosity and crack density on the compressive strength of rocks. *Int. J. Rock Mech. Min. Sci.* 67, 202–211.
- Bažant, Z.P., 2004. Scaling theory for quasibrittle structural failure. *Proc. Natl. Acad. Sci.* 101, 13400–13407. <http://dx.doi.org/10.1073/pnas.0404096101>.
- Bell, A.F., Kilburn, C.R.J., 2013. Trends in the aggregated rate of pre-eruptive volcano-tectonic seismicity at Kilauea volcano, Hawaii. *Bull. Volcanol.* 75, 677. <http://dx.doi.org/10.1007/s00445-012-0677-y>.
- Bell, A.F., Kilburn, C.R.J., 2012. Precursors to dyke-fed eruptions at basaltic volcanoes: insights from patterns of volcano-tectonic seismicity at Kilauea volcano, Hawaii. *Bull. Volcanol.* 74, 325–339.
- Bell, A.F., Naylor, M., Heap, M.J., Main, I.G., 2011. Forecasting volcanic eruptions and other material failure phenomena: an evaluation of the failure forecast method. *Geophys. Res. Lett.* 38, L15304. <http://dx.doi.org/10.1029/2011gl048155>.
- Bell, A.F., Naylor, M., Main, I.G., 2013. The limits of predictability of volcanic eruptions from accelerating rates of earthquakes. *Geophys. J. Int.* 194, 1541–1553. <http://dx.doi.org/10.1093/gji/ggt191>.
- Blair, S.C., Berge, P.A., Berryman, J.G., 1993. Two-Point Correlation Functions to Characterize Microgeometry and Estimate Permeabilities of Synthetic and Natural Sandstones. Lawrence Livermore National Lab., CA (United States).
- Boué, A., Lesage, P., Cortés, G., Valette, B., Reyes-Dávila, G.A., 2015. Real-time eruption forecasting using the material Failure Forecast Method with a Bayesian approach. *J. Geophys. Res.* 120, 2143–2161.
- Castro, J., Cashman, K., Joslin, N., Olmsted, B., 2002. Structural origin of large gas cavities in the Big Obsidian Flow, Newberry Volcano. *J. Volcanol. Geotherm. Res.* 114, 313–330.
- Cornelius, R., Scott, P., 1993. A materials failure relation of accelerating creep as empirical description of damage accumulation. *Rock Mech. Rock Eng.* 26, 233–252.
- De la Cruz-Reyna, S., Reyes-Dávila, G.A., 2001. A model to describe precursory material-failure phenomena: applications to short-term forecasting at Colima volcano, Mexico. *Bull. Volcanol.* 63, 297–308. <http://dx.doi.org/10.1007/s004450100152>.
- Goodier, J., 1933. Concentration of stress around spherical and cylindrical inclusions and flaws. *J. Appl. Mech.* 1, 39–44.
- Guyer, E.P., Dauskardt, R.H., 2004. Fracture of nanoporous thin-film glasses. *Nat. Mater.* 3, 53–57. <http://dx.doi.org/10.1557/jmr.2006.0106>.
- Hao, S., Liu, C., Lu, C., Elsworth, D., 2016. A relation to predict the failure of materials and potential application to volcanic eruptions and landslides. *Sci. Rep.* 6, 27877.
- Hatton, C.G., Main, I.G., Meredith, P.G., 1994. Non-universal scaling of fracture length and opening displacement. *Nature* 367, 160–162. <http://dx.doi.org/10.1038/367160a0>.
- Heap, M., Mollo, S., Vinciguerra, S., Lavallée, Y., Hess, K.-U., Dingwell, D., Baud, P., Lezzi, G., 2013. Thermal weakening of the carbonate basement under Mt. Etna volcano (Italy): implications for volcano instability. *J. Volcanol. Geotherm. Res.* 250, 42–60.
- Heap, M.J., Farquharson, J.I., Wadsworth, F.B., Kolzenburg, S., Russell, J.K., 2015. Timescales for permeability reduction and strength recovery in densifying magma. *Earth Planet. Sci. Lett.* 429, 223–233.
- Jaeger, J., Cook, N., Zimmerman, R., 2009. *Fundamentals of Rock Mechanics*. Wiley.
- Jiang, X., Jiang, D., Chen, J., Salje, E., 2016. Collapsing minerals: crackling noise of sandstone and coal, and the predictability of mining accidents. *Am. Mineral.* 101, 2751–2758.
- Kemeny, J., Cook, N., 1986. Effective moduli, non-linear deformation and strength of a cracked elastic solid. *Int. J. Rock Mech. Min. Sci.* 23, 107–118.
- Kendrick, J.E., Lavallée, Y., Hirose, T., di Toro, G., Hornby, A.J., de Angelis, S., Dingwell, D.B., 2014. Volcanic drumbeat seismicity caused by stick-slip motion and magmatic frictional melting. *Nat. Geosci.* 7, 438–442. <http://dx.doi.org/10.1038/NGEO2146>.
- Kilburn, C., De Natale, G., Carlino, S., 2017. Progressive approach to eruption at Campi Flegrei caldera in southern Italy. *Nat. Commun.* 8.
- Kilburn, C.R.J., 2012. Precursory deformation and fracture before brittle rock failure and potential application to volcanic unrest. *J. Geophys. Res.* 117, B02211. <http://dx.doi.org/10.1029/2011JB008703>.
- Kilburn, C.R.J., 2003. Multiscale fracturing as a key to forecasting volcanic eruptions. *J. Volcanol. Geotherm. Res.* 125, 271–289. [http://dx.doi.org/10.1016/s0377-0273\(03\)00117-3](http://dx.doi.org/10.1016/s0377-0273(03)00117-3).
- Kilburn, C.R.J., Voight, B., 1998. Slow rock fracture as eruption precursor at Soufriere Hills volcano, Montserrat. *Geophys. Res. Lett.* 25, 3665–3668. <http://dx.doi.org/10.1029/98gl01609>.
- Kirsch, G., 1898. *Die theorie der elastizität und die bedürfnisse der festigkeitslehre*. Springer.
- Lamb, O., Angelis, S., Wall, R., Lamur, A., Varley, N., Reyes-Dávila, G., Arámbula-Mendoza, R., Hornby, A., Kendrick, J., Lavallée, Y., 2017. Seismic and experimental insights into eruption precursors at Volcán de Colima. *Geophys. Res. Lett.* 44.
- Lavallée, Y., Benson, P.M., Heap, M.J., Hess, K.-U., Flaws, A., Schillinger, B., Meredith, P.G., Dingwell, D.B., 2013. Reconstructing magma failure and the degassing network of dome-building eruptions. *Geology* 41, 515–518. <http://dx.doi.org/10.1130/G33948.1>.
- Lavallée, Y., Meredith, P.G., Dingwell, D.B., Hess, K.-U., Wassermann, J., Cordonnier, B., Gerik, A., Kruhl, J.H., 2008. Seismogenic lavas and explosive eruption forecasting. *Nature* 453, 507–510. <http://dx.doi.org/10.1038/nature06980>.
- Lockner, D., Byerlee, J., Kukensko, V., 1991. Quasi-static fault growth and shear fracture energy in granite. *Nature* 350, 39–42.
- Lu, B., Torquato, S., 1992. Nearest-surface distribution functions for polydispersed particle systems. *Phys. Rev. A* 45, 5530–5544.
- Neuberg, J.W., Tuffen, H., Collier, L., Green, D., Powell, T., Dingwell, D.B., 2006. The trigger mechanism of low-frequency earthquakes on Montserrat. *J. Volcanol. Geotherm. Res.* 153, 37–50. <http://dx.doi.org/10.1016/j.jvolgeores.2005.08.008>.
- Ortiz, R., Moreno, H., García, A., Fuentealba, G., Astiz, M., Peña, P., Sánchez, N., Tárrega, M., 2003. Villarrica volcano (Chile): characteristics of the volcanic tremor and forecasting of small explosions by means of a material failure method. *J. Volcanol. Geotherm. Res.* 128, 247–259.
- Robertson, R., Kilburn, C., 2016. Deformation regime and long-term precursors to eruption at large calderas: Rabaul, Papua New Guinea. *Earth Planet. Sci. Lett.* 438, 86–94.
- Salvage, R., Neuberg, J.W., 2016. Using a cross correlation technique to refine the accuracy of the Failure Forecast Method: application to Soufrière Hills volcano, Montserrat. *J. Volcanol. Geotherm. Res.* 324, 118–133. <http://dx.doi.org/10.1016/j.jvolgeores.2016.05.011>.
- Sammis, C.G., Ashby, M.F., 1986. The failure of brittle porous solids under compressive stress states. *Acta Metall.* 34, 511–526. [http://dx.doi.org/10.1016/0001-6160\(86\)90087-8](http://dx.doi.org/10.1016/0001-6160(86)90087-8).
- Scholz, C., 1968. Experimental study of the fracturing process in brittle rock. *J. Geophys. Res.* 73, 1447–1454.
- Smith, R., Kilburn, C.R.J., 2010. Forecasting eruptions after long repose intervals from accelerating rates of rock fracture: the June 1991 eruption of Mount Pinatubo, Philippines. *J. Volcanol. Geotherm. Res.* 191, 129–136. <http://dx.doi.org/10.1016/j.jvolgeores.2010.01.006>.
- Smith, R., Kilburn, C.R.J., Sammonds, P.R., 2007. Rock fracture as a precursor to lava dome eruptions at Mount St Helens from June 1980 to October 1986. *Bull. Volcanol.* 69, 681–693. <http://dx.doi.org/10.1007/s00445-006-0102-5>.
- Sornette, D., Andersen, J.V., 1998. Scaling with respect to disorder in time-to-failure. *Eur. Phys. J. B* 1, 353–357. <http://dx.doi.org/10.1007/s100510050194>.
- Soutas-Little, R., 1999. *Elasticity*. Courier Corporation.
- Torquato, S., 2013. *Random Heterogeneous Materials: Microstructure and Macroscopic Properties*. Springer Science & Business Media.
- Torquato, S., Lu, B., Rubinstein, J., 1990. Nearest-neighbour distribution function for systems on interacting particles. *J. Phys. A* 23, L103.
- Turcotte, D., Newman, W., 2003. Micro and macroscopic models of rock fracture. *Geophys. J. Int.* 152, 718–728.
- Vasseur, J., Wadsworth, F.B., Lavallée, Y., Bell, A.F., Main, I.G., Dingwell, D.B., 2015. Heterogeneity: the key to failure forecasting. *Sci. Rep.* 5, 13259. <http://dx.doi.org/10.1038/srep13259>.
- Vasseur, J., Wadsworth, F.B., Lavallée, Y., Dingwell, D.B., 2016. Dynamic elastic moduli during isotropic densification of initially granular media. *Geophys. J. Int.* 204, 1721–1728. <http://dx.doi.org/10.1093/gji/ggv550>.

- Vasseur, J., Wadsworth, F.B., Lavallée, Y., Hess, K.U.K.-U., Dingwell, D.B., 2013. Volcanic sintering: timescales of viscous densification and strength recovery. *Geophys. Res. Lett.* 40, 5658–5664. <http://dx.doi.org/10.1002/2013GL058105>.
- Voight, B., 1989. A relation to describe rate-dependent material failure. *Science* 80 (243), 200–203. <http://dx.doi.org/10.1126/science.243.4888.200>.
- Voight, B., 1988. A method for prediction of volcanic eruptions. *Nature* 332, 125–130.
- Voight, B., Cornelius, R.R., 1991. Prospects for eruption prediction in near real-time. *Nature* 350, 695–698.
- Wadsworth, F.B., Heap, M.J., Dingwell, D.B., 2016. Friendly fire: engineering a fort wall in the Iron Age. *J. Archaeol. Sci.* 67, 7–13.
- Zhu, W., Baud, P., Vinciguerra, S., Wong, T.-F., 2011. Micromechanics of brittle faulting and cataclastic flow in Alban Hills tuff. *J. Geophys. Res.* 116, B06209.